Oxidation-assisted graphene heteroepitaxy on copper foil

Nicolas Reckinger, Xiaohui Tang, Frederic Joucken, Luc Lajaunie, Raul Arenal, Emmanuel Dubois, Benoit Hackens, Luc Henrarda, Jean-Francois Colomer

Oxidation-assisted graphene heteroepitaxy on copper foil

Nicolas Reckinger,*[a,b] Xiaohui Tang,[c] Frédéric Joucken,[a,b] Luc Lajaunie,[d] Raul Arenal,[d,e] Emmanuel Dubois,[f] Benoît Hackens,[g] Luc Henrard[a,b] and Jean-François Colomer[a,b]

DOI: 10.1039/c6nr02936a

We propose an innovative, easy-to-implement approach to synthesize aligned large-area single-crystalline graphene flakes by chemical vapor deposition on copper foil. This method doubly takes advantage of residual oxygen present in the gas phase. First, by slightly oxidizing the copper surface, we induce grain boundary pinning in copper and, in consequence, the freezing of the thermal recrystallization process. Subsequent reduction of copper under hydrogen suddenly unlocks the delayed reconstruction, favoring the growth of centimeter-sized copper (111) grains through the mechanism of abnormal grain growth. Second, the oxidation of the copper surface also drastically reduces the nucleation density of graphene. This oxidation/reduction sequence leads to the synthesis of aligned millimeter-sized monolayer graphene domains in epitaxial registry with copper (111). The as-grown graphene flakes are demonstrated to be both single-crystalline and of high quality.

Introduction

Chemical vapor deposition (CVD) holds great promises for large-scale production of high-quality graphene. The very low carbon solubility in copper (Cu) makes it a very attractive catalyst for graphene CVD growth.[1] Low-pressure CVD leads to the self-limited growth of a graphene monolayer[2] while the same outcome can be obtained by atmospheric pressure CVD (APCVD) provided that the amount of injected hydrocarbon is carefully controlled (by working with highly diluted hydrocarbons for instance).[3] However, graphene sheets produced by standard CVD on Cu are polycrystalline[2] and domain boundaries have a detrimental effect on transport properties of charge carriers in graphene.[4] Besides, large-scale single-crystalline monolayer graphene sheets constitute optimal building blocks for artificial layer stacking with a precise control of the interlayer rotation angle. Twisted bilayer graphene, formed from the stacking of two monolayer graphene sheets, has already demonstrated a range of interesting optoelectronic behaviors.[5–8]

One approach to grow large-size graphene domains is a drastic lowering of the graphene nucleation density by various techniques such as: growth on resolidified Cu,[9] on Cu annealed at high pressure,[10] or by local feeding of carbon precursors.[11] The most popular method involves a superficial oxidation of Cu to suppress nucleation.[12–16] A recent study provides solid arguments to attribute this effect to the removal of carbon contamination on the Cu surface rather than to the presence of oxygen.[17]

The Cu(111) surface plane is very advantageous for graphene synthesis because its hexagonal lattice symmetry matches well the honeycomb lattice of graphene (lattice mismatch of ~4%), thereby enabling epitaxial graphene growth. It is also attractive for the efficient decoupling of CVD graphene from Cu[18] in the context of transfer methods yielding high-mobility graphene-based solid-state devices.[19] A few publications (see Table S1† for more details) report on the formation of large Cu(111) grains spanning several millimeters starting from polycrystalline foils,[9,16,20] after annealing at temperatures close to the melting point of Cu (1088 °C), where the grain boundary mobility is high. After such thermal treatments, Cu naturally adopts the (111) crystallographic orientation since it is thermodynamically the most stable for face-

[a]Research Group on Carbon Nanostructures (CARBONNAGe), University of Namur, Rue de Bruxelles 61, 5000 Namur, Belgium. E-mail: nicolas.reckinger@unamur.be, nicolas.reckinger@gmail.com

[b]Department of Physics, Research Center in Physics of Matter and Radiation (PMR), University of Namur, Rue de Bruxelles 61, 5000 Namur, Belgium

[c]ICTEAM, Université catholique de Louvain (UCL), Place du Levant 3, 1348 Louvain-la-Neuve, Belgium

[d]Laboratorio de Microscopías Avanzadas (LMA), Instituto de Nanociencia de Aragón (INA), Universidad de Zaragoza, 50018 Zaragoza, Spain

[e]ARAID Foundation, 50018 Zaragoza, Spain

[f]UMR CNRS 8520, IEMN/ISEN, Avenue Poincaré, BP 60069, 59652 Villeneuve d'Ascq Cedex, France

[g]Institute of Condensed Matter and Nanosciences/Nanoscopic Physics, Université catholique de Louvain (UCL), Chemin du Cyclotron 2, 1348 Louvain-la-Neuve, Belgium

†Electronic supplementary information (ESI) available. See DOI: 10.1039/c6nr02936a

centered cubic metals.[21,22] By contrast, Robinson *et al.*[22] report the formation of large Cu grains with a dominant (001) texture, the initial main orientation of the Cu foil. Following this line of thought, a novel method has emerged recently, in addition to the "single-domain" one. It consists in orienting the surface of initially polycrystalline Cu foils along the (111) orientation by long (several hours) thermal annealing at more than 1000 °C. The subsequent epitaxial growth of graphene conduces to the alignment of domains which ultimately merge to form a graphene film free of domain boundaries over several dozen centimeter squares.[23,24] Other more expensive, complicated techniques imply directly working on Cu(111) single crystals[25–27] or depositing a thin layer of Cu epitaxially oriented on α-Al_2O_3(0001)[28–30] or MgO(111) substrates.[31]

The mechanism underlying the growth of large grains in materials is known as abnormal grain growth.[32,33] Cold-rolled metal foils are polycrystalline in nature. After annealing at high temperature, the process of primary recrystallization results in the formation of new dislocation-free grains. When subjected to further annealing at high temperature, the average grain size continues to increase because it is thermodynamically more favorable to reduce the total grain boundary energy. Gradually, larger grains grow at the expense of smaller ones *via* grain boundary migration (normal grain growth). In specific conditions, normal grain growth may give way to abnormal grain growth where a selective growth of a few "giant" grains occurs by absorbing the small neighboring ones. Abnormal grain growth can only proceed if normal grain growth is somehow inhibited, notably by grain boundary pinning.[32]

In this work, we describe a new method, merging the advantages of the "single-domain" and epitaxial growth approaches, where we take advantage of residual oxygen in the gas phase. First, by slightly oxidizing the Cu surface, we induce grain boundary pinning and, in consequence, freezing of the thermal recrystallization process. Subsequent reduction of Cu under hydrogen suddenly unlocks the delayed reconstruction, favoring abnormal grain growth over normal grain growth. This results in the centimeter-scale reconstruction of the Cu substrate along the surface plane (111) orientation. The identification of abnormal grain growth as the mechanism responsible for the Cu reconstruction is the main novelty and the crux of our work. The posterior adjunction of methane leads to the aligned growth of large-area monolayer graphene domains. Compared to the usual hydrogen pre-growth annealing, this oxidation/reduction sequence is thus doubly beneficial: (1) the (111) reconstruction of Cu foils at the centimeter scale is greatly accelerated, allowing graphene domains to grow in an aligned way through epitaxial registry with the Cu substrate and, (2) the oxidation drastically reduces the nucleation density and promotes the growth of millimeter-sized monolayer graphene flakes.

Experimental

Graphene growth

We start from Cu foil pieces with a size of 3 × 3 cm^2 (Alfa Aesar, reference number 13382: 25 μm-thick, purity 99.8%). The Cu pieces are cleaned in a 2 : 1 mixture of acetic acid and distilled water (see ESI section 16† for more details), rinsed in distilled water, and blown-dry with nitrogen. For the growth, the sample is first put on a quartz boat and inserted into a quartz tube at room temperature. An argon flow of 2000 sccm is then fed into the tube for 15 min and the temperature of the hotwall furnace is increased to 1050 °C. Next, the quartz tube is introduced into the furnace and the argon flow decreased to 500 sccm, with the immediate or delayed addition of 20 sccm of hydrogen. After 1 h in these conditions, dilute methane (5% in 95% of argon) is injected to grow graphene. The quartz tube is extracted 1 h later from the furnace and left to cool down naturally in the same gas mixture.

Graphene transfer

Graphene is transferred onto 300 nm-thick silicon dioxide/silicon substrates or TEM grids (Ted Pella, #01896N) by the widely used method based on poly(methyl methacrylate) (PMMA). After PMMA coating, the Cu foil is first partially etched in ammonium persulfate to remove graphene grown on the backside. After rinsing and rubbing the backside with a cleanroom wiper, the foil's etching is continued in a fresh persulfate solution. The PMMA/graphene stack is next rinsed thoroughly in distilled water and fished on the wanted support. The sample is left to dry overnight and, finally, PMMA is removed with acetone.

Additional details regarding the experimental techniques (scanning electron microscopy, energy-dispersive X-ray spectroscopy, electron-backscattering diffraction, low-energy electron diffraction, X-ray photoelectron spectroscopy, micro-Raman spectroscopy, transmission electron microscopy) can be found in the ESI section 17.†

Results and discussion

The temperature-time diagram shown in Fig. 1a summarizes the so-called "standard" (small, misaligned domains) and novel (macroscopic, aligned domains) graphene growth conditions, with the corresponding argon and hydrogen flows. The unique difference between the two processes is the pre-growth annealing of the Cu foils: (1) a **reductive** annealing under argon and hydrogen[2–4,13] (dubbed S#1:H_2/S#2:H_2, see Fig. 1a for the notations) or (2) an **oxidative**/**reductive** annealing under argon, then argon and hydrogen[12,13,15,16] (S#1:**noH_2**/S#2:H_2). The results of the two pre-growth sequences are compared in the low magnification scanning electron microscopy (SEM) images displayed in Fig. 1b and c. We observe that the slightly different thermal treatments result in radically dissimilar Cu foil morphologies. It is indeed clearly seen in Fig. 1b that the S#1:H_2/S#2:H_2 Cu foil is polycrystalline, as testified by the heterogeneous SEM contrast rendered by the diverse Cu grain orientations, due to electron channeling. On the other hand, the other Cu foil exhibits a nearly uniform contrast, as in Fig. 1c (except for white lines due the rolling striations, darker contrast due to curving of the foil, and a few

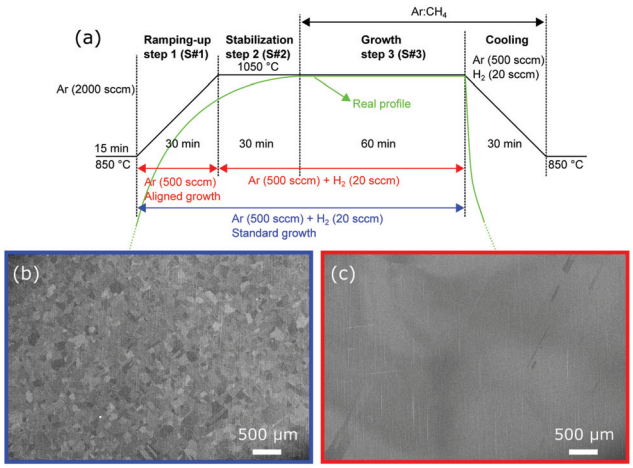

Fig. 1 (a) Temperature-time diagram summarizing the different steps of the standard (in blue) and aligned (in red) graphene growth conditions with the corresponding argon and hydrogen flows. Scanning electron microscopy pictures of Cu foils after (b) S#1:H_2/S#2:H_2 (highlighted in blue) or (c) S#1:noH_2/S#2:H_2 (highlighted in red).

elongated grains). The systematic use of low magnification SEM to completely sweep the surface of three 3 × 3 cm^2 S#1:noH_2/S#2:H_2 foils suggests the same qualitative conclusion: the foils present an almost completely unique crystallographic orientation. However, a few residual polycrystalline areas are seen, most of the time on the edges of the foil (Fig. S1a and b†), or where it is strongly deformed (Fig. S1c and d†). In line with that observation, the reconstruction proves unstable on the edges of pieces cut from reconstructed 3 × 3 cm^2 samples when they are heated once again in the same conditions (Fig. S1e and g†). Strain created during the cutting causes the foil to return to a polycrystalline state on the edges. These observations evidence that deformations in the Cu foil play a very important role in the reconstruction. It is also noteworthy that the reconstruction is not purely superficial but rather extends throughout the whole thickness of the Cu foil, as proven by the SEM inspection of both sides of a reconstructed Cu foil (Fig. S2†). In a final control experiment, it is found out that an annealing under argon and hydrogen of at least four hours is necessary to reconstruct a 3 × 3 cm^2 Cu foil in a similar manner to the S#1:noH_2/S#2:H_2 treatment (Fig. S3†), meaning that the oxidative/reductive annealing helps to drastically shorten the recrystallization duration and consequently the cost of the whole process.

To unambiguously identify the crystalline structure and determine the size of the Cu grains, we perform electron-backscattering diffraction. First, the analysis of a 3 × 1 cm^2 S#1:H_2/S#2:H_2 Cu stripe (cut from a 3 × 3 cm^2 Cu piece) shows that it is mainly (001)-oriented, as illustrated in Fig. 2a displaying the corresponding out-of-plane inverse pole figure (IPF) map (with the IPF on the right). The Cu(001) orientation was already reported by other works for Cu foils subjected to similar treatments.[20,34] Then, a 3 × 1 cm^2 S#1:noH_2/S#2:H_2 Cu stripe (also cut from a 3 × 3 cm^2 Cu piece) is investigated in three distinct regions (see Fig. 2b exhibiting a photograph of the stripe with color-coded circles locating the three analyzed areas in the center and on the two edges). The corresponding IPF maps exposed in Fig. 2c–h give a confirmation of the large-scale (111) reconstruction of the Cu substrate (with the associated IPF in inset). More precisely, the uniform color in each out-of-plane IPF map is representative of a completely (111)-oriented Cu surface (Fig. 2c–e), while the uniform color in each in-plane IPF map shows that there is no rotational misfit (*i.e.* no twinning) between the three spots (Fig. 2f–h), so that the three areas belong to the same Cu crystal. The slight color variations that we can see in Fig. 2c and e reflect the uneven topography of the foil (local corrugations or larger-scale creases, as seen in Fig. 2b), meaning that, in places, the normal to the investigated surface is not exactly at the right angle with respect to the detector. On the other hand, the IPF map in Fig. 2d is very uniform and the crystallographic orientation much closer to the (111) pole (see the corresponding IPF) because the Cu foil in the center is much flatter. The only observed non-uniformities are the elongated grains that could already be seen previously in the SEM pictures in Fig. 1c. These small-sized rare grains are identified as (001)-oriented (Fig. S4†), in agreement with ref. 23.

We now investigate the mechanism responsible for accelerating abnormal grain growth (see an illustration of abnormal grain growth in Fig. S5†). The sole difference between the two pre-growth annealings considered here is the suppression of hydrogen during S#1. In the absence of hydrogen and its reducing effect, it is known that trace amounts of oxygen are inevitably present in the atmosphere and affect CVD growth.[35,36] In consequence, we are naturally led to believe that oxygen plays a major role in the reconstruction of the Cu foil. To shed more light on the oxidation of Cu, energy-dispersive X-ray spectroscopy (EDX) mapping is conducted on a Cu piece after the S#1:noH_2 thermal treatment (complementary X-ray photoelectron spectroscopy data can be found in Fig. S6a–d†). The SEM image in Fig. 3a reveals that the surface of the foil is scattered with micrometer-sized faceted inclusions, formed preferentially on the Cu grain boundaries. The corresponding EDX O K and Cu K elemental mappings (Fig. 3b and c) disclose that oxygen is almost entirely concentrated in the crystalline inclusions, with a ~33% atomic concentration, matching the stoichiometry of Cu_2O; while the dark background corresponds to very weakly oxidized Cu, with less than 1.5% in oxygen (see the corresponding spectra in Fig. S7a and b†). In Fig. 3d, micro-Raman spectroscopy (μRS) further corroborates that the spectrum recorded on the particles corresponds to Cu_2O[14,37] and that the background is weakly oxidized. Besides, the Ellingham diagram for the Cu/O_2 couple ($4Cu + O_2 \leftrightarrow 2Cu_2O$) confirms that Cu_2O is stable under the considered O_2 partial pressure and temperature conditions (see ESI section 9† for more details).[38] Finally, in two complementary control experiments, we see that the average Cu grain size is not altered after prolonged (see Fig. 3e–g and ESI section 10†) or repeated (Fig. S8a and b†) S#1:noH_2 annealings, proving that the recrystallization is frozen.

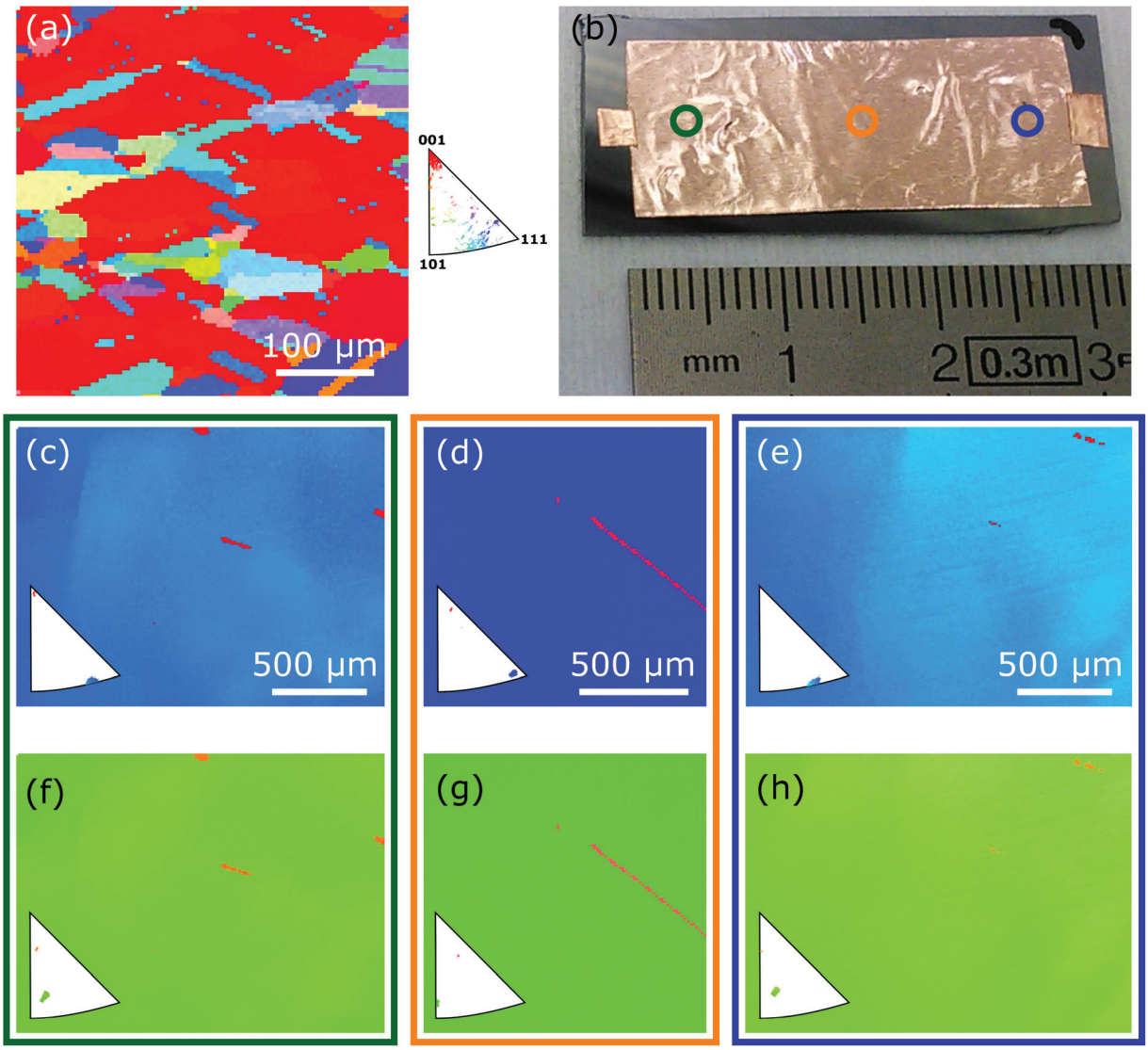

Fig. 2 (a) Electron-backscattering diffraction out-of-plane inverse pole figure map of a Cu sample after S#1:H_2/S#2:H_2. (b) Photograph of a 3 × 1 cm^2 Cu stripe cut from a 3 × 3 cm^2 piece after S#1:noH_2/S#2:H_2, with three colored circles locating where the maps are recorded. Electron-backscattering diffraction out-of-plane (c–e) and in-plane (f–h) inverse pole figure maps at the three locations, with a frame colored according to the circles in (b). The corresponding inverse pole figure is in inset to each inverse pole figure map.

Based on the knowledge gained through the previous experiments, we propose the following scenario. During the first minutes of annealing under argon, the grain boundary mobility is high enough to enable the average Cu grain size to increase under the effect of the temperature (primary recrystallization). The conditions of temperature and residual oxygen partial pressure evolve in such a way that they become favorable to the formation of Cu_2O inclusions. These particles end up pinning down the Cu grain boundaries, even provoking the stagnation of the recrystallization. These conditions are very propitious to abnormal grain growth.[32] So, when hydrogen is introduced in the reactor and the Cu grains are suddenly unpinned, the recrystallization is strongly driven to proceed by abnormal grain growth.

After unveiling the mechanism underlying the trigger of abnormal grain growth, we further investigate the growth of graphene on the (111)-reconstructed Cu foils. The standard conditions (growth following S#1:H_2/S#2:H_2) lead to misaligned, monolayer graphene domains with a lateral size of 10–15 μm (apex to apex) as can be seen in the SEM image displayed in Fig. 4a. This is commonly reported in the literature for graphene synthesized without any special pretreatment of the Cu foil.[3,13] Not content with accelerating the (111) reconstruction, the S#1:noH_2/S#2:H_2 pre-growth conditions also result in a spectacular size enlargement of the graphene flakes[13] beyond 1 millimeter (compared to 50–100 μm for Brown *et al.*[23] and Nguyen *et al.*[24]), and very interestingly, the different graphene domains are aligned (Fig. 4b). By contrast,

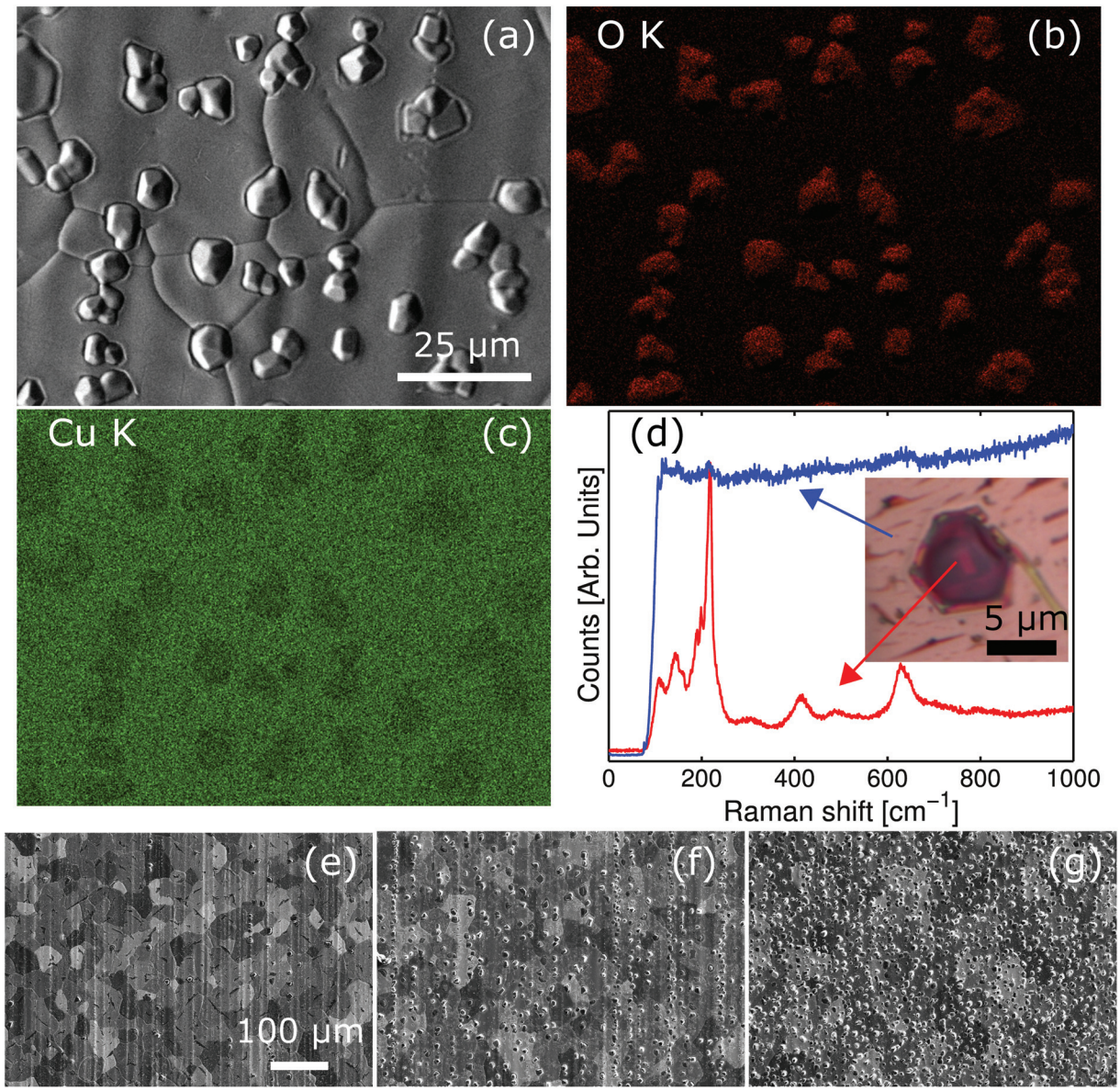

Fig. 3 Scanning electron microscopy image (a), energy-dispersive X-ray spectroscopy O K (b) and Cu K (c) mappings of a Cu foil after S#1:noH_2. (d) Micro-Raman spectrum of a Cu_2O inclusion shown by optical microscopy in the insert. Surface of three Cu foils annealed for (e) 30 min, (f) 1 h or (g) 2 h in argon only.

unlike Zhou *et al.*,[14] it is found that the reverse pre-growth sequence (S#1:H_2/S#2:noH_2) leads to a much higher nucleation density, resulting in smaller hexagons (<50 μm) and in multilayer patches (Fig. S9†). This is most probably due to a much higher number of Cu oxide particles formed during S#2:noH_2 which are preferential sites for graphene nucleation.[39] Annealing in hydrogen has indeed a short range polishing effect on the Cu foil,[13,40] smoothing out Cu oxide particles and others defects (rolling striations, *etc.*), thereby strongly decreasing the nucleation density (Fig. S10†). The top part of Fig. 4c gives an additional illustration of merged graphene flakes aligned growth over ~7 mm (it is composed of two low magnification SEM pictures stitched together). As mentioned in the ESI (Fig. S1†), the edges of the foil remains polycrystalline due to mechanical strain. Consequently, the graphene domains are inevitably misaligned at these locations. In the inset to Fig. 4c, we also show one representative low-energy electron diffraction pattern acquired on the same sample (three others are available in Fig. S11†). They all display a single set of diffraction spots corresponding to the hexagonal symmetry of both the Cu(111) and graphene lattices aligned with each other. The small lattice mismatch and the relatively large size of the diffraction spots due to the uneven foil prevents from resolving the graphene and Cu(111) diffraction spots, as reported by Brown *et al.*[23] The diffraction data strongly support the epitaxial align-

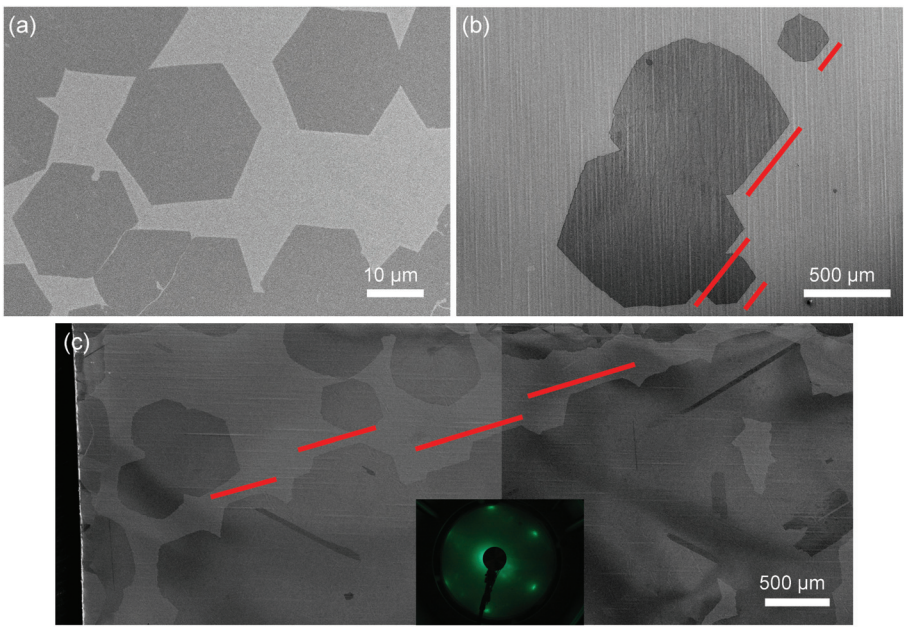

Fig. 4 Scanning electron microscopy (SEM) image of graphene flakes grown on Cu after (a) S#1:H_2/S#2:H_2 or (b) S#1:noH_2/S#2:H_2. (c) SEM picture illustrating graphene alignment at the centimeter scale. Inset: low-energy electron diffraction pattern taken on the sample.

ment between the quasi-monocrystalline Cu(111) foil and graphene.

Next, we evaluate the structural quality of the as-grown graphene flakes by μRS. Fig. 5a exhibits a 800 μm-wide hexagonal graphene flake transferred onto a Si/SiO_2 (300 nm-thick) substrate. Fig. 5b–e presents the corresponding μRS mappings of the 2D-band full width at half maximum (Γ_{2D} = 25.8 ± 1.4 cm^{-1}), the 2D-band shift (ω_{2D} = 2684.4 ± 0.8 cm^{-1}), the G-band shift (ω_G = 1582 ± 1.1 cm^{-1}), and the ratio between the 2D and G integrated intensities (I_{2D}/I_G = 2.3 ± 0.5). The values of each figure of merit match the typical values of high-quality CVD-grown monolayer graphene.[2,13,14] In Fig. S12,† we plot 10 full spectra recorded at random locations on the sample. From these spectra, one can barely distinguish the defect-related D band located at 1350 cm^{-1} (in some points, it is even not visible), testimony to the very good structural

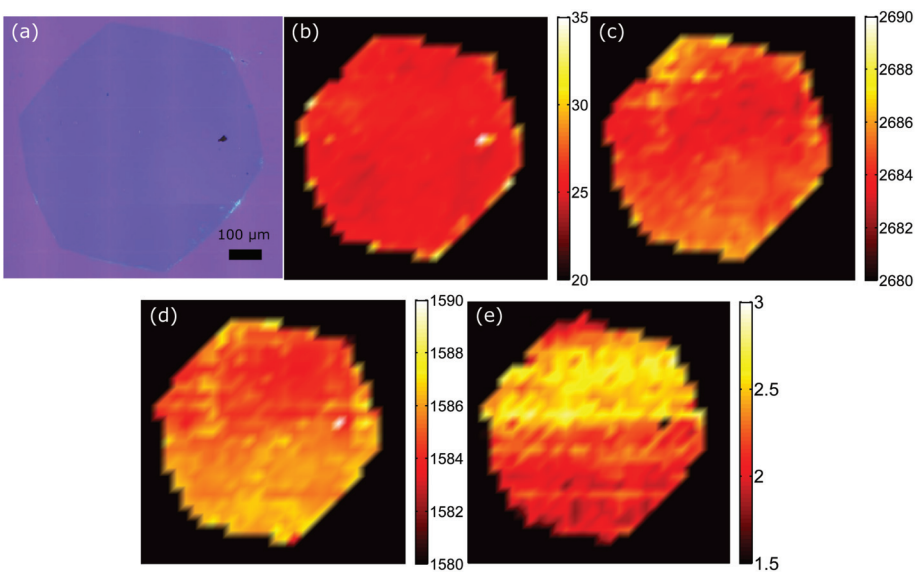

Fig. 5 (a) Optical microscopy picture of a 800 μm-sized monolayer graphene domain transferred onto a Si/SiO_2 substrate. Corresponding micro-Raman spectroscopy mappings of the (b) 2D-band full width at half maximum, (c) 2D-band shift, (d) G-band shift, and (e) 2D-band over G-band integrated intensity ratio.

quality of the graphene flakes. Comparing our data with values for suspended exfoliated monolayer graphene, taken as a reference for unperturbed graphene ($\Gamma_{2D} \approx 22$ cm^{-1}, $\omega_{2D} \approx 2677$ cm^{-1}),[41] we can see that Γ_{2D} (25.8 cm^{-1}) is very slightly broadened and ω_{2D} (2684.4 cm^{-1}) is weakly upshifted. The Γ_{2D} broadening can be the sign of doping (arising from the SiO_2 substrate, from contaminations over and/or under graphene, from moisture, *etc.*), while it can also reflect the averaging of nanometer-scale strain variations in the graphene flakes.[41–43] The ω_{2D} stiffening can also be attributed to doping and strain in graphene.[41] Disentangling the two effects is difficult since CVD graphene is unavoidably strained and doped. Likewise, the spread on the data can be ascribed to local variations in doping and strain.

Nanobeam electron diffraction (ED) analyses by transmission electron microscopy (TEM) are also performed to demonstrate the single-crystalline nature of the graphene flakes.[44,45] Fig. 6a shows an optical microscopy picture of a 1300 μm-wide hexagonal graphene flake covered by a poly(methyl methacrylate) support film, transferred onto a TEM grid. Up to 25 ED patterns are acquired through the holes of the TEM grid (Fig. S13†). Fig. 6b displays some of the most representative ED patterns. All of them correspond to monolayer single crystalline graphene oriented along the [0001] zone axis. No evidence of extended defects or turbostratic multilayers can be inferred from these data. Fig. 6c plots the evolution of the δ angle (angle between the [0–110] plane and the horizontal axis, see Fig. 6b) with the covered path. Along the pathway (seen in Fig. 6a) covering more than 4.3 mm, the δ values are centered on a mean value of 63.2 ± 0.6° (with a 95% confidence interval). This confirms the good crystallinity and the single crystalline nature of the monolayer graphene flake on its entire area. Both μRS and TEM testify to the excellent quality and spatial uniformity both of the graphene synthesis and the transfer process.

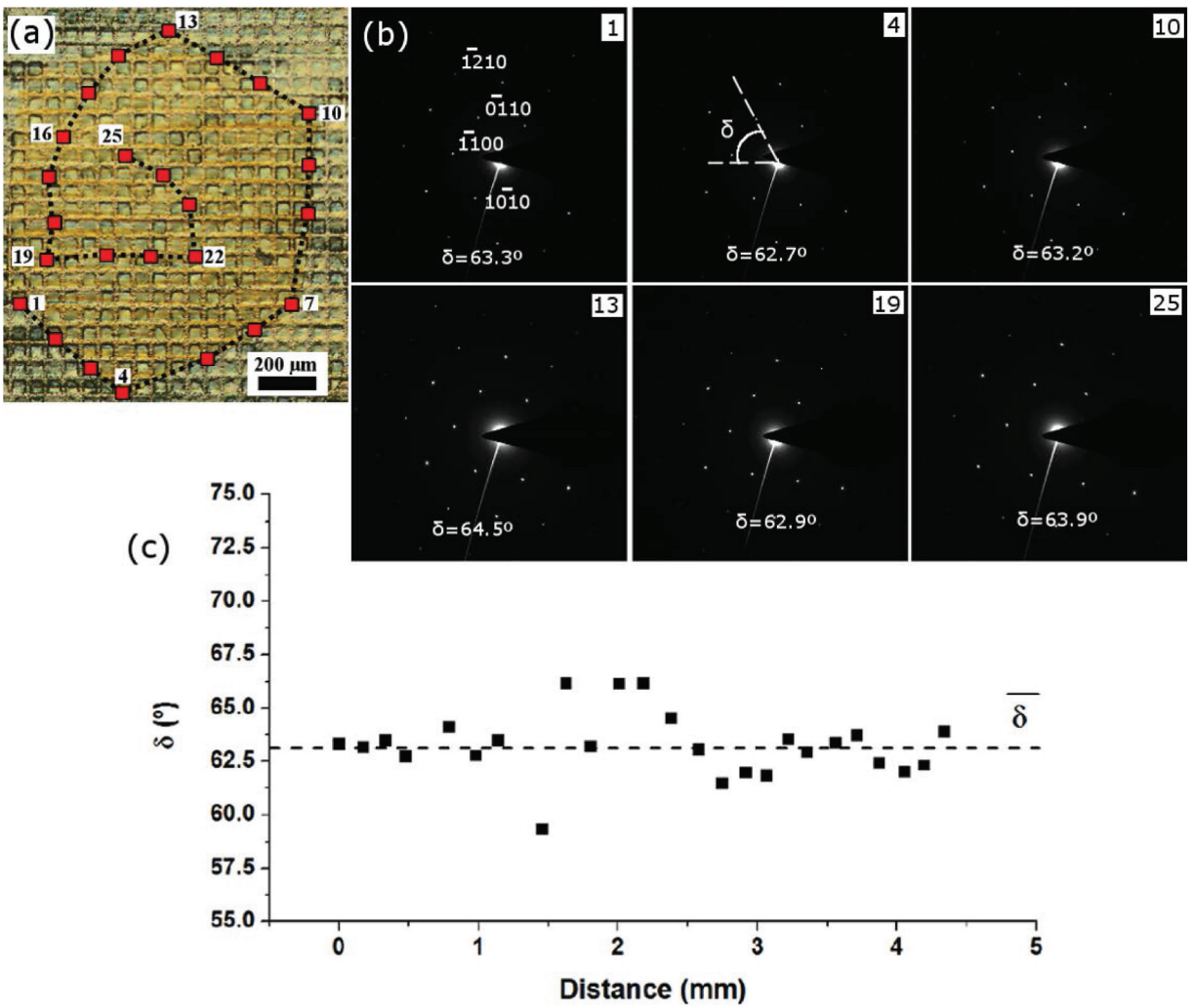

Fig. 6 (a) Optical microscopy image of a 1.3 mm-sized monolayer graphene hexagon covered with poly(methyl methacrylate) transferred onto a transmission electron microscopy grid. Red squares highlight the areas where the 25 corresponding electron diffraction (ED) analyses are performed. (b) The most representative ED patterns, labeled according to the analyzed area. (c) Variation of the δ angle along the covered pathway shown by the dotted line in (a).

Conclusions

The present work details an innovative method to grow single-crystalline graphene sheets by CVD, where residual oxygen in the gas phase proves to be doubly advantageous. The superficial oxidation of cold-rolled polycrystalline Cu foils simultaneously (1) accelerates the foil recrystallization in the (111) orientation and (2) drastically lowers the nucleation density. Growing graphene on such Cu(111) templates leads to high-quality monolayer single-crystalline graphene flakes spanning more than 1 millimeter, aligned at the centimeter scale.

Crucially, we reveal abnormal grain growth as the mechanism underlying the Cu reconstruction. Combined with other techniques, it can prove useful in the endeavor towards full control and understanding of graphene CVD growth.

Acknowledgements

The authors acknowledge P. Jacques and A. Vlad for helpful discussions. They also acknowledge P. Louette, F. Ureña, C. Charlier, and C. Boyaval for their help during the experiments. The research leading to this work received funding from the European Union Seventh Framework Program under grant agreement No 604391 Graphene Flagship. The TEM studies were conducted at the Laboratorio de Microscopias Avanzadas, Instituto de Nanociencia de Aragon, Universidad de Zaragoza, Spain. Some of the research leading to these results has also received funding from the European Union Seventh Framework Programme under Grant Agreement 312483-ESTEEM2 (Integrated Infrastructure Initiative – I3), as well as from EU H2020 ETN project "Enabling Excellence" Grant Agreement 642742 and the Spanish Ministerio de Economia y Competitividad (FIS2013-46159-C3-3-P). This work is partially supported by the Multi-Sensor-Platform for Smart Building Management project (No. 611887). This research used resources of the Electron Microscopy Service at the University of Namur ("Plateforme Technologique Morphologie – Imagerie"). This research also used resources of the ELISE Service of the University of Namur. This service is member of the "Plateforme Technologique SIAM". Part of this work was financially supported by the Actions de Recherche Concertées (ARC) "StressTronics" and "NATURIST".

References

1 G. A. López and E. J. Mittemeijer, *Scr. Mater.*, 2009, **51**, 1.
2 X. Li, W. Cai, J. An, S. Kim, J. Nah, D. Yang, R. Piner, A. Velamakanni, I. Jung, E. Tutuc, S. K. Banerjee, L. Colombo and R. S. Ruoff, *Science*, 2009, **324**, 1312.
3 I. Vlassiouk, M. Regmi, P. Fulvio, S. Dai, P. Datskos, G. Eres and S. Smirnov, *ACS Nano*, 2011, **5**, 6069.
4 Q. Yu, L. A. Jauregui, W. Wu, R. Colby, J. Tian, Z. Su, H. Cao, Z. Liu, D. Pandey, D. Wei, T. F. Chung, P. Peng, N. P. Guisinger, E. A. Stach, J. Bao, S.-S. Pei and Y. P. Chen, *Nat. Mater.*, 2011, **10**, 443.
5 Y. Wang, Z. Ni, L. Liu, Y. Liu, C. Cong, T. Yu, X. Wang, D. Shen and Z. Shen, *ACS Nano*, 2010, **4**, 4074.
6 R. W. Havener, H. Zhuang, L. Brown, R. G. Hennig and J. Park, *Nano Lett.*, 2012, **12**, 3162.
7 R. He, T.-F. Chung, C. Delaney, C. Keiser, L. A. Jauregui, P. M. Shand, C. C. Chancey, Y. Wang, J. Bao and Y. P. Chen, *Nano Lett.*, 2013, **13**, 3594.
8 J. Yin, H. Wang, H. Peng, Z. Tan, L. Liao, L. Lin, X. Sun, A. L. Koh, Y. Chen, H. Peng and Z. Liu, *Nat. Commun.*, 2016, **7**, 10699.
9 A. Mohsin, L. Liu, P. Liu, W. Deng, I. N. Ivanov, G. Li, O. E. Dyck, G. Duscher, J. R. Dunlap, K. Xiao and G. Gu, *ACS Nano*, 2013, **7**, 8924.
10 Z. Yan, J. Lin, Z. Peng, Z. Sun, Y. Zhu, L. Li, C. Xiang, E. L. Samuel, C. Kittrell and J. M. Tour, *ACS Nano*, 2012, **6**, 9110.
11 T. Wu, X. Zhang, Q. Yuan, J. Xue, G. Lu, Z. Liu, H. Wang, H. Wang, F. Ding, Q. Yu, X. Xie and M. Jiang, *Nat. Mater.*, 2015, **15**, 43.
12 Y. Hao, M. S. Bharathi, L. Wang, Y. Liu, H. Chen, S. Nie, X. Wang, H. Chou, C. Tan, B. Fallahazad, H. Ramanarayan, C. W. Magnuson, E. Tutuc, B. I. Yakobson, K. F. McCarty, Y.-W. Zhang, P. Kim, J. Hone, L. Colombo and R. S. Ruoff, *Science*, 2013, **342**, 720.
13 L. Gan and Z. Luo, *ACS Nano*, 2013, **7**, 9480.
14 H. Zhou, W. J. Yu, L. Liu, R. Cheng, Y. Chen, X. Huang, Y. Liu, Y. Wang, Y. Huang and X. Duan, *Nat. Commun.*, 2013, **4**, 3096.
15 G. Eres, M. Regmi, C. M. Rouleau, J. Chen, I. N. Ivanov, A. A. Puretzky and D. B. Geohegan, *ACS Nano*, 2014, **8**, 5657.
16 V. Miseikis, D. Convertino, N. Mishra, M. Gemmi, T. Mashoff, S. Heun, N. Haghighian, F. Bisio, M. Canepa, V. Piazza and C. Coletti, *2D Mater.*, 2015, **2**, 014006.
17 J. Kraus, M. Böbel and S. Günther, *Carbon*, 2016, **96**, 153.
18 K. Wong, S. J. Kang, C. W. Bielawski, R. S. Ruoff and S. K. Kwak, *J. Am. Chem. Soc.*, 2016, **138**, 10986.
19 L. Banszerus, M. Schmitz, S. Engels, J. Dauber, M. Oellers, F. Haupt, K. Watanabe, T. Taniguchi, B. Beschoten and C. Stampfer, *Sci. Adv.*, 2015, **1**, e1500222.
20 A.-Y. Lu, S.-Y. Wei, C.-Y. Wu, Y. Hernandez, T.-Y. Chen, T.-H. Liu, C.-W. Pao, F.-R. Chen, L.-J. Li and Z.-Y. Juang, *RSC Adv.*, 2012, **2**, 3008.
21 Y.-N. Wen and J.-M. Zhang, *Solid State Commun.*, 2007, **144**, 163.
22 Z. R. Robinson, P. Tyagi, T. M. Murray, C. A. Ventrice, S. Chen, A. Munson, C. W. Magnuson and R. S. Ruoff, *J. Vac. Sci. Technol., A*, 2012, **30**, 011401.
23 L. Brown, E. B. Lochocki, J. Avila, C.-J. Kim, Y. Ogawa, R. W. Havener, D.-K. Kim, E. J. Monkman, D. E. Shai, H. I. Wei, M. P. Levendorf, M. Asensio, K. M. Shen and J. Park, *Nano Lett.*, 2014, **14**, 5706.
24 V. L. Nguyen, B. G. Shin, D. L. Duong, S. T. Kim, D. Perello, Y. J. Lim, Q. H. Yuan, F. Ding, H. Y. Jeong, H. S. Shin,

S. M. Lee, S. H. Chae, Q. A. Vu, S. H. Lee and Y. H. Lee, *Adv. Mater.*, 2015, **27**, 1376.
25 L. Gao, J. R. Guest and N. P. Guisinger, *Nano Lett.*, 2010, **10**, 3512.
26 S. Gottardi, K. Müller, L. Bignardi, J. C. Moreno-López, T. A. Pham, O. Ivashenko, M. Yablonskikh, A. Barinov, J. Björk, P. Rudolf and M. Stöhr, *Nano Lett.*, 2015, **15**, 917.
27 Z. R. Robinson, P. Tyagi, T. R. Mowll, C. A. Ventrice and J. B. Hannon, *Phys. Rev. B: Condens. Matter*, 2012, **86**, 235413.
28 K. M. Reddy, A. D. Gledhill, C.-H. Chen, J. M. Drexler and N. P. Padture, *Appl. Phys. Lett.*, 2011, **98**, 113117.
29 D. L. Miller, M. W. Keller, J. M. Shaw, A. N. Chiaramonti and R. R. Keller, *J. Appl. Phys.*, 2012, **112**, 064317.
30 B. Hu, H. Ago, Y. Ito, K. Kawahara, M. Tsuji, E. Magome, K. Sumitani, N. Mizuta, K. Ikeda and S. Mizuno, *Carbon*, 2012, **50**, 57.
31 Y. Ogawa, B. Hu, C. M. Orofeo, M. Tsuji, K. Ikeda, S. Mizuno, H. Hibino and H. Ago, *J. Phys. Chem. Lett.*, 2012, **3**, 219.
32 F. J. Humphreys and M. Hatherly, *Recrystallization and Related Annealing Phenomena*, Elsevier, Oxford, England, 2nd edn, 2004, ch. 11.
33 T. Omori, T. Kusama, S. Kawata, I. Ohnuma, Y. Sutou, Y. Araki, K. Ishida and R. Kainuma, *Science*, 2013, **341**, 1500.
34 J. M. Wofford, S. Nie, K. F. McCarty, N. C. Bartelt and O. D. Dubon, *Nano Lett.*, 2010, **10**, 4890.
35 N. Reckinger, A. Felten, C. N. Santos, B. Hackens and J.-F. Colomer, *Carbon*, 2013, **63**, 84.
36 S. Choubak, M. Biron, P. L. Levesque, R. Martel and P. Desjardins, *J. Phys. Chem. Lett.*, 2013, **4**, 1100.
37 J. Dawson, M. M. Hargreave and G. R. Wilkinson, *J. Phys. Chem. Solids*, 1973, **34**, 2201.
38 P. Atkins and J. de Paula, *Physical Chemistry, Volume 1: Thermodynamics and Kinetics*, W. H. Freeman & Co, New York, US, 8th edn, 2008.
39 T. Liang, G. He, G. Huang, Y. Kong, W. Fu, H. Chen, Q. Wang, H. Iwai, D. Fujita, Y. Liu and M. Xu, *Adv. Mater.*, 2015, **27**, 6404.
40 H. Wang, G. Wang, P. Bao, S. Yang, W. Zhu, X. Xie and W.-J. Zhang, *J. Am. Chem. Soc.*, 2012, **134**, 3627.
41 J. E. Lee, G. Ahn, J. Shim, Y. S. Lee and S. Ryu, *Nat. Commun.*, 2012, **3**, 1024.
42 C. Neumann, S. Reichardt, P. Venezuela, M. Drögeler, L. Banszerus, M. Schmitz, K. Watanabe, T. Taniguchi, F. Mauri, B. Beschoten, S. V. Rotkin and C. Stampfer, *Nat. Commun.*, 2015, **6**, 8429.
43 C. Casiraghi, S. Pisana, K. S. Novoselov, A. K. Geim and A. C. Ferrari, *Appl. Phys. Lett.*, 2007, **91**, 233108.
44 R. Arenal, M. Kociak, A. Loiseau and D.-J. Miller, *Appl. Phys. Lett.*, 2006, **89**, 073104.
45 D. Levshov, T. X. Than, R. Arenal, V. N. Popov, R. Parret, M. Paillet, V. Jourdain, A. A. Zahab, T. Michel, Y. I. Yuzyuk and J.-L. Sauvajol, *Nano Lett.*, 2011, **11**, 4800.